



# Ni, In co-doped ZnIn<sub>2</sub>S<sub>4</sub> for efficient hydrogen evolution: Modulating charge flow and balancing H adsorption/desorption

Dongxue Zhou<sup>a,b,1</sup>, Xiangdong Xue<sup>a,1</sup>, Xing Wang<sup>a,b</sup>, Qingjie Luan<sup>a,b</sup>, Ang Li<sup>c,\*</sup>,  
Liguo Zhang<sup>a,b</sup>, Baozhen Li<sup>a,b</sup>, Wenjun Dong<sup>a,b,\*\*</sup>, Ge Wang<sup>a,\*</sup>, Changmin Hou<sup>d</sup>

<sup>a</sup> Beijing Advanced Innovation Center for Materials Genome Engineering, Beijing Key Laboratory of Function Materials for Molecule & Structure Construction, School of Materials Science and Engineering, University of Science and Technology Beijing, Beijing 100083, PR China

<sup>b</sup> Shunde Graduate School of University of Science and Technology Beijing, Foshan 528399, PR China

<sup>c</sup> School of Materials Science and Engineering, Suzhou University of Science and Technology, Suzhou 215009, PR China

<sup>d</sup> State Key Laboratory of Inorganic Synthesis & Preparative Chemistry, College of Chemistry, Jilin University, Changchun 130012, PR China

## ARTICLE INFO

### Keywords:

Ni, In co-doping  
ZnIn<sub>2</sub>S<sub>4</sub>  
Potential wells  
H adsorption/desorption  
Photocatalyst

## ABSTRACT

Element doping is an excellent strategy to promote charge separation and reaction kinetics of photocatalyst, which plays significant role in accelerating the sustainable energy development process. Herein, Ni, In co-doped ZnIn<sub>2</sub>S<sub>4</sub> photocatalyst was prepared by a microwave-assisted solvothermal method. The rapid crystallization of ZnIn<sub>2</sub>S<sub>4</sub> resulted in partial In atoms substituted Zn atom during the formation of [ZnS]<sub>4</sub> layer. In doping in tetrahedral Zn sites increases the electron delocalization around In sites, hence reduces the electronic potential wells along Z axis. Ni doping in tetrahedral Zn sites decreases the negative charge on the S sites, which balances the H adsorption/desorption, further boosting the photocatalytic activity. As a result, Ni, In co-doped ZnIn<sub>2</sub>S<sub>4</sub> possess an optimal photocatalytic H<sub>2</sub> evolution property of 21.94 μmol·h<sup>-1</sup>, which is nearly 1.8 and 6.1 times of In-ZnIn<sub>2</sub>S<sub>4</sub> (11.78 μmol·h<sup>-1</sup>) and ZnIn<sub>2</sub>S<sub>4</sub> (3.6 μmol·h<sup>-1</sup>).

## 1. Introduction

Hydrogen (H<sub>2</sub>) has attracted extensive attention to alleviate the global energy crisis, serving as a sustainable energy resource [1–5]. Especially, photocatalytic water splitting into hydrogen is convincing as an intriguing route for transform solar-light energy to chemical energy [1,3,5]. Metal chalcogenide semiconductors [6–8], including ZnS [9], CdS [10–13], PbS [14], Co<sub>9</sub>S<sub>8</sub> [15,16], ZnIn<sub>2</sub>S<sub>4</sub> [17–20], exhibit favorable photocatalytic H<sub>2</sub> production property due to the strong visible-light response ability and appropriate energy band structure. Particularly, ZnIn<sub>2</sub>S<sub>4</sub> has aroused keen interest due to its suitable band gap (2.2–2.6 eV), environmental friendliness and the prominent photo-stability [21].

Layered structure ZnIn<sub>2</sub>S<sub>4</sub> consists of alternate stacking structure, containing S-Zn-S-In-S-In-S along Z axis [22,23]. Owing to the different charge density of each layer, a periodic electronic potential exists in the ZnIn<sub>2</sub>S<sub>4</sub> crystal, resulting in a series of potential wells [22,24]. As a

result, the potential wells impede the photoexcited carriers transfer along Z axis. For a half unit cell ZnIn<sub>2</sub>S<sub>4</sub>, the orbital distribution of the valence band maximum (VBM) and the conduction band minimum (CBM) are mainly localized on surface [ZnS]<sub>4</sub> layer and [InS]<sub>4</sub> layer, respectively [21,25,26]. The unique 2D ultrathin structure effectively shortens the diffusion distance and promotes the photogenerated charges transfer to active sites, boosting photocatalytic H<sub>2</sub> evolution. During photoexcitation, photogenerated electrons would transfer from VBM at [ZnS]<sub>4</sub> surface layer to CBM at the [InS]<sub>4</sub> surface layer, and the electrons pass through the potential wells, arriving the active sites to participate the reduction reaction. Hence, the potential wells of ZnIn<sub>2</sub>S<sub>4</sub> block the photoexcited electrons traveling along Z axis, and then result in low charges separation and transport efficiency.

In order to optimize the charge flow along Z axis of ZnIn<sub>2</sub>S<sub>4</sub>, many strategies have been pursued to promote the charge separation and transport [21,27,28]. For example, constructing ultrathin structure endow a shortened charge transfer distance, and reduce the

\* Corresponding authors.

\*\* Corresponding author at: Beijing Advanced Innovation Center for Materials Genome Engineering, Beijing Key Laboratory of Function Materials for Molecule & Structure Construction, School of Materials Science and Engineering, University of Science and Technology Beijing, Beijing 100083, PR China.

E-mail addresses: [angli@ustb.edu.cn](mailto:angli@ustb.edu.cn) (A. Li), [wdong@ustb.edu.cn](mailto:wdong@ustb.edu.cn) (W. Dong), [gewang@mater.ustb.edu.cn](mailto:gewang@mater.ustb.edu.cn) (G. Wang).

<sup>1</sup> These authors contributed equally to this work.

recombination for the photoexcited carriers [20,29,30]. The enhanced charge separation and transport dramatically promote photocatalytic  $H_2$  evolution property. In addition, cocatalyst loading or heterojunction are effective strategies to tune the charge flow [14,17,27,31,32]. For instance,  $MoS_2$  quantum dots selectively loaded near S vacancies of monolayer  $ZnIn_2S_4$ , inducing the electrons divert along Z axis [25]. The S vacancies accumulated the photoexcited electron, and then the electrons quickly migrated from monolayer  $ZnIn_2S_4$  to  $MoS_2$ . The electron transmitted along opposite Z axis, thereby not passed the potential wells in ZIS and improved the efficiency of separation. Actually, the ultrathin nanosheets design or subtle atomic-level heterostructure strategy cannot modulate the intrinsic potential wells in  $ZnIn_2S_4$ , the electrons excited from VBM to CBM is still blocked by the intrinsic potential wells, which greatly decrease the photocatalytic reaction efficiency.

In this paper, the Ni, In co-doped  $ZnIn_2S_4$  (denoted as NiIn-ZIS) catalyst was synthesized by a microwave-assisted solvothermal method. The microwave synthesis induced a rapid heating rate, the ultrafast crystallization of  $ZnIn_2S_4$  resulted in partial In atoms substituted Zn atom during the formation of  $[ZnS]_4$  layer. In term of the NiIn-ZIS catalyst, In doping reduces electronic potential wells and Ni doping modulates the H absorption/desorption ability. In doping in tetrahedral Zn sites increases the electron delocalization around In sites, hence reduces the electronic potential wells along Z axis and increases the conductivity of NiIn-ZIS. The reduced electronic potential and increased conductivity endow the rapid charges separation and transport. On the other side, Ni dopant crucially affects the H adsorption capabilities for hydrogen evolution reaction. The Ni doping in tetrahedral Zn sites induces an increased H adsorption behavior on S sites, which modulates the H absorption ability and balances the H adsorption/desorption. As a result, the Ni, In co-doped  $ZnIn_2S_4$  catalyst possess an optimal photocatalytic  $H_2$  evolution property of  $21.94 \mu\text{mol}\cdot\text{h}^{-1}$ , which is nearly 1.8 and 6.1 times of In- $ZnIn_2S_4$  ( $11.78 \mu\text{mol}\cdot\text{h}^{-1}$ ) and  $ZnIn_2S_4$  ( $3.6 \mu\text{mol}\cdot\text{h}^{-1}$ ). This work affords an available inspiration on promoting the photoexcited charges separation/transport and balancing H absorption/desorption by controllable doping tactics to signally boost the photocatalytic performance.

## 2. Experimental section

### 2.1. Chemical

Zinc chloride ( $ZnCl_2$ , 99.999%), indium chloride hydrate ( $InCl_3\cdot 4H_2O$ , 98%), thioacetamide ( $C_2H_5NS$ , 99%), nickel (II) chloride hexahydrate ( $NiCl_2\cdot 6H_2O$ ) and triethanolamine (TEOA) were bought from Aladdin. N, N-Dimethylformamide (DMF) and ethylene glycol (EG) were bought from Sinopharm Chemical Reagent Co. Ltd. (China). All chemicals were used without further purification.

### 2.2. Materials preparation

Synthesis of In doped  $ZnIn_2S_4$  assembled ultrathin nanosheets. In doped ZIS was prepared by a microwave-assisted solvothermal method. Typically,  $ZnCl_2$  (0.5 mmol, 68 mg) and  $InCl_3\cdot 4H_2O$  (1 mmol, 293.2 mg) were added in 60 mL DMF and 4 mL EG and ultrasonicated to dissolve it evenly. Subsequently, TAA (2 mmol, 150 mg) was added. After stirring in well, the mixture was transferred to a 100 mL two-neck flask and placed in MCR-3A Atmospheric Microwave chemical reactor. The parameters of the microwave reaction were 90 s and  $150^\circ\text{C}$ . The obtained samples were denoted as In-ZIS.

Synthesis of Ni, In co-doped  $ZnIn_2S_4$ . To prepare Ni-doped In-ZIS, 1.5, 2, 2.5 and 3 mL 0.1 M  $NiCl_2\cdot 6H_2O$  EG solution were added into the mixed In-ZIS precursor solution before transferring into the flask. The remaining steps are the same as the synthesis of In-ZIS. Finally, the obtained samples were denoted as NiIn-ZIS.

Synthesis of bulk  $ZnIn_2S_4$ . The bulk ZIS was synthesized by a hydrothermal method.  $ZnCl_2$  (0.2 mmol, 27.2 mg),  $InCl_3\cdot 4H_2O$  (0.2 mmol,

58.6 mg) and TAA (0.4 mmol, 30 mg) were dissolved in 8 mL of  $H_2O$  (pH = 2.5) and 2 mL of glycerol with vigorous stirring for 30 min. Then the resulting mixture was placed into a water bath at  $80^\circ\text{C}$  under stirring for 2 h.

### 2.3. Characterization

The micro-morphologies of the prepared samples were observed by the Scanning electron microscope (SEM, Hitachi SU 8010) and transmission electron microscope (TEM, JEM-2200FS). The aberration-corrected high-resolution high-angle annular dark-field scanning transmission electron microscopy (HAADF-STEM) was applied to obtained the atomic arrangement. X-ray diffraction (XRD) pattern was recorded on X-ray diffraction instrument (Bruker D8 Advanced) operating at 40 KV and 40 mA with  $Cu\text{-}K\alpha$  radiation. The UV-vis diffuse reflectance spectra were acquired on a Shimadzu UV-3600 UV-Vis-NIR spectrophotometer and  $BaSO_4$  reference. Photoluminescence (PL) spectra were read-in by a Fluorescence Spectrophotometer (Hitachi F-7000). Decay curves were obtained on a FLS980 fluorescence lifetime spectrophotometer (Edinburgh Instruments, UK) under the excitation wavelength at 325 nm. The average lifetime (Ave.  $\tau$ ) is calculated according to  $\tau = (A_1\bullet\tau_1^2 + A_2\bullet\tau_2^2) / (A_1\bullet\tau_1 + A_2\bullet\tau_2)$  ( $\tau_i$  is the lifetime;  $A_i$  is the relative intensity). The ratios of element were analyzed by the inductively coupled plasma-atomic emission spectrometer (ICP-AES) on PerkinElmer Optima 7300DV. An ESCALAB 250Xi electron spectrometer with Mg  $K\alpha$  (1253.6 eV) source was performed to characterize the X-ray photoelectron spectroscopy. The materials were degassed in vacuum at  $120^\circ\text{C}$ , and then measured at 77 K to test  $N_2$  sorption. The electron paramagnetic resonance spectrometer (Model EMX-10/12 X-band, Bruker, Germany) was applied to collect the electron paramagnetic resonance (EPR) spectrum.

Electrochemical workstation (CHI660D) equipped with a typical three-electrode cell was used to evaluate photo-electrochemical performance. In the three-electrode cell, Pt sheet was used as the counter electrode and Ag/AgCl was used as the reference electrode. The working electrodes were prepared by oneself. The procedures as follows: 10 mg of the photocatalyst was dispersed into the mixed solution of 450  $\mu\text{L}$  ethanol and 50  $\mu\text{L}$  Nafion to make uniform slurry. Then, the slurry was coated onto the surface of the FTO glass electrodes, dried at room temperature.

### 2.4. Computational details

The linear combination of atomic orbitals (LCAO) method was employed to perform the spin unrestricted DFT simulations [33–36]. The exchange-correlation effects were deal within generalized gradient approximation with the Perdew-Burke-Ernzerhof (GGA-PBE). DFT Semi-core Pseudopotentials (DSPPs) and a double numerical plus polarization set were selected computational accuracy. Special k-points sampling integration over the Brillouin zone was employed by using the Monkhorst-Pack scheme. The orbital cut-off quality of 5 Å and the k-point grid of  $4 \times 4 \times 1$  were applied for a slab model containing a 14-atom layer and a 15 Å vacuum. The convergence criterion for force, energy and displacement were set to  $5.0 \times 10^{-5}$  Ha, 0.002 Ha/Å, and 0.005 Å, respectively, while  $1.0 \times 10^{-7}$  Ha was chosen for electronic minimization. During the optimization of structures, both atomic positions and the cell were fully relaxed.

### 2.5. Photocatalytic activity test

The PHE experiments were estimated in a closed stainless reactor (volume: 54 mL) with a top window for visible-light irradiation. 2 mg prepared photocatalyst was dispersed in 10 mL 10% TEOA aqueous solution in a Pyrex flask. The closed reactor was degassing pretreatment for 30 min. The photocatalytic reaction started after irradiation and the production of  $H_2$  was analyzed using gas chromatograph (GC-2014,

TCD). Except the activity, the stability of the photocatalyst was evaluated by the recycle test. The apparent quantum efficiency (AQE) was detected under irradiation with various band-pass filter including 400, 420, 500 and 550 nm, respectively. A 300 W Xe-lamp equipped with an UV cut-off filter ( $\lambda \geq 420$  nm) was adopted as the light source.

### 3. Result and discussion

#### 3.1. Characterization of the photocatalysts

In microwave-assisted solvothermal synthesis, the dielectric loss factor of the solvent represents the ability to absorb microwaves, which can greatly affect the heating and crystallization rate [37–40]. In the hydrothermal method, due to the bond order (B) relationship ( $B_{[\text{In-S}]}$  in  $[\text{InS}]_6$  interlayer <  $B_{[\text{In-S}]}$  in  $[\text{InS}]_4$  surface layer <  $B_{[\text{Zn-S}]}$  in  $[\text{ZnS}]_4$  surface layer), so the tetrahedron  $[\text{ZnS}]_4$  layer is easily formed than  $[\text{InS}]_6$  and  $[\text{InS}]_4$  layers. As a result, In substituted tetrahedron Zn sites is hard to realize with a the hydrothermal method due to the rapid formation of  $[\text{ZnS}]_4$  layer [41]. The introduction of ethylene glycol with high dielectric loss factor into the microwave system results in a rapid heating rate and an ultrafast crystallization process (Fig S1). Thus, partial In atoms substituted Zn atom during the formation of  $[\text{ZnS}]_4$  layer (denoted as In-ZIS), accompanied with inevitable disordered atomic arrangement in crystal during the ultrafast crystallization process. Subsequently, Ni doped In-ZIS was produced after the addition of

Ni ions in the solution (NiIn-ZIS). Morphology and structure of the NiIn-ZIS and the pristine  $\text{ZnIn}_2\text{S}_4$  (denoted as ZIS) samples are systematically characterized. X-ray diffraction (XRD) results confirm In-ZIS and NiIn-ZIS are hexagonal structure, which are similar as  $\text{ZnIn}_2\text{S}_4$  (JCPDS file No. 65-2023) [23]. The characteristic peaks at  $21.59^\circ$ ,  $27.69^\circ$ ,  $47.18^\circ$  and  $55.58^\circ$  can be indexed to (006), (102), (110) and (022) planes, respectively (Fig. 1a). In contrast to ZIS, all peaks of In-ZIS shift to the low angle especially the (006) and (102) peaks, due to the larger atomic radius of In atom (1.66) than that of Zn atom (1.39). No evidently diffraction peaks shift is detected after Ni introduction due to the tiny content of Ni element. The flower-like NiIn-ZIS microsphere composes by multiple ultrathin nanosheets (Fig. 1d and e). The thickness of nanosheets for NiIn-ZIS and ZIS are approximately 1.3–1.4 nm (Fig. 1b and c) and 2.3–3.3 nm (Fig. S2), respectively. It suggests that the NiIn-ZIS nanosheet is a half-unit-cell slab along the Z axis. The loosely stacked structure achieves a high specific surface area ( $131.50 \text{ m}^2/\text{g}$  of NiIn-ZIS and  $55.08 \text{ m}^2/\text{g}$  of ZIS), which provides abundant active sites for photocatalytic hydrogen evolution (Fig. S3).

The transmission electron microscopy (TEM) image demonstrates the transparent ultrathin morphology for NiIn-ZIS nanosheets (Fig. 1e). The high-resolution TEM (HRTEM) image uncovers the 0.33 nm interplanar distance in the sample match well with  $d_{100}$  spacings and the interaxial angles of  $60^\circ$  of the hexagonal phase ZIS (Fig. 1f). XRD and HRTEM results show no  $\text{NiS}_x$  nanoparticles are formed in the NiIn-ZIS. The lattice fringe twist in NiIn-ZIS illustrate the dopant induced the

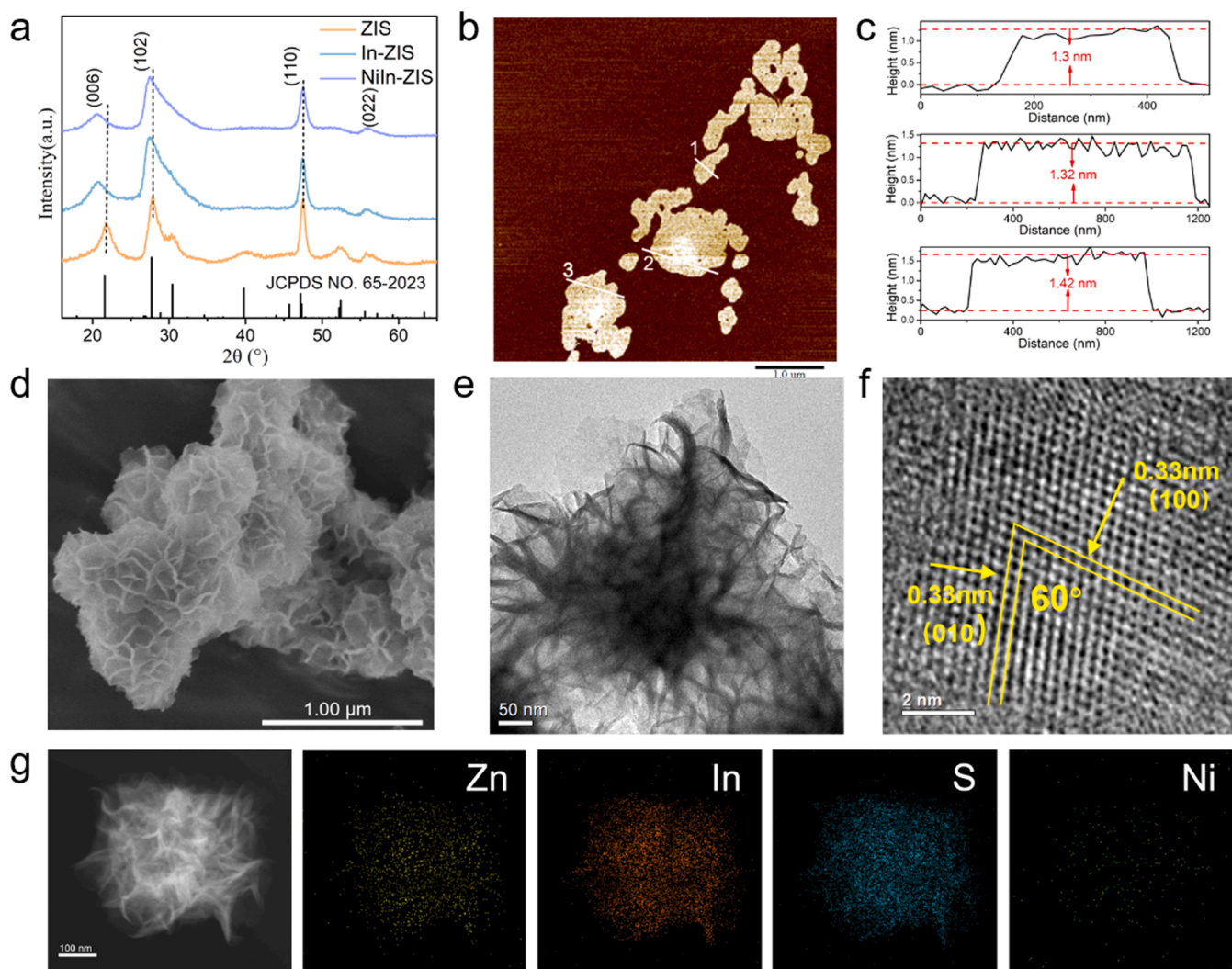


Fig. 1. (a) XRD patterns of NiIn-ZIS, In-ZIS and ZIS, (b), (c) AFM, (d) SEM, (e) TEM, (f) HRTEM and (g) EDX-mapping of NiIn-ZIS.



lattice distortion (Fig. S5). The STEM-energy dispersive X-ray (EDX) mapping of NiIn-ZIS suggests the existence of Zn, In, S and Ni. In, Zn and S elements disperse uniformly, while the Ni distributes sporadically due to the minimal Ni doping. The density distribution of Zn for NiIn-ZIS is evidently lower than that for ZIS (Fig. S4), the Zn/In/S molar ratio of NiIn-ZIS is 0.57:2.23:4 (Table S1), which illustrate the deficiency of Zn in NiIn-ZIS nanosheets. The enriched In atom and minimal Ni atom (0.37 wt%, Table S1) doping induce the lattice distortion and change the electronic structure.

HAADF-STEM result reveals the atomic arrangements in the half-unit-cell  $\text{ZnIn}_2\text{S}_4$  layer (Fig. 2a and b). It is well known the In atom can be easily distinguished from Zn by the size and brightness [21,42,43]. The magnified image convincingly manifests partial Zn sites are substituted by In atoms (Fig. 2c). Normally, Zn atoms (dark spots) locate in the center of regular hexagon, which is consisted by six In atoms (bright spots). After the In doping, the hexagon occurs distort and the partial centered Zn atoms (dark spots) are substituted by In atoms (bright spots). Whereas, Ni atoms are indistinguishable from Zn atoms owing to the similar atomic number between Zn and Ni. The Ni atom could replace Zn atoms in NiIn-ZIS for the similar electronic configuration and atomic radius between Ni and Zn atom [44,45]. Furthermore, the disordered atomic arrangements in some regions illustrate the existence of crystal defects. The EPR response at 2.003 g-value confirms Ni doping further increased the defects in NiIn-ZIS (Fig. S6). In brief, the Ni, In co-doped  $\text{ZnIn}_2\text{S}_4$ , in which partial Zn atoms are substituted by In and Ni atoms on  $[\text{ZnS}]_4$  layer simultaneously, was obtained by a simple microwave-assisted solvothermal synthesis method. In and Ni doping regulate the electronic structure of NiIn-ZIS and then improve the photocatalytic property of the catalyst.

In order to make in-depth understanding of the local structure and coordination environment of Zn, In, S and Ni elements in NiIn-ZIS, X-ray absorption near edge structure (XANES) and extended X-ray absorption fine structure (EXAFS) techniques are employed to define the subtle atomic structure. Compared with ZIS, Zn K-edge for In-ZIS XANES spectroscopy shows the near-edge absorption energy shifts to higher energy level (Fig. 3a). Meanwhile, the near-edge absorption energy of S K-edge XANES spectroscopy shift to low energy direction (Fig. 3b). The Zn K-edge and S K-edge shifts of near-edge absorption energy indicate the In doping changes the electron structure in the crystal. Based on the Fourier transformed (FT)  $k^3$ -weighted EXAFS spectra and the least squares EXAFS curve-fitting, the FT EXAFS spectra of In-ZIS verifies the In doping configuration and the related parameters are listed in Fig. 3 and Table S2 [2,23]. In the  $R$ -space EXAFS spectrum, the stretched Zn-S bond (2.33 Å) of In-ZIS confirms that In doping induced structure distortion with respect to the Zn-S bond (2.31 Å) of ZIS (Table S2). In the second coordination shell around Zn of ZIS, the coordination number of 6 is correspond to the scattering contribution of Zn-Zn. While in In-ZIS,

the coordination number of 3 is correspond the scattering contribution of Zn-Zn and another coordination number of 3 is assigned to the Zn-In scattering coordination. The appearance of Zn-In bond in second shell illustrates the In doping in the tetrahedral Zn sites. The Wavelet transfer (WT) EXAFS plots confirmed the exist of Zn-In bond [46,47]. The Zn-M scattering paths of In-ZIS show a stronger signal compared to ZIS, which is contributed by the cooperation of Zn-Zn and Zn-In (Fig. 3e-h). In addition, the Ni K-edge XANES spectra of the NiIn-ZIS is obviously different from that of Ni foil, which exclude Ni particle or cluster exist in NiIn-ZIS (Fig. S8 and Table S3). The Fourier transformed (FT)  $k^3$ -weighted EXAFS spectra of NiIn-ZIS identifies the bond length is 2.26 Å and the coordination number is 4, which assigned to Ni-S<sub>4</sub> tetrahedral structure. In summary, the XAFS analysis of Zn, In, Ni and S proves the successfully introduction of In and Ni atom doped into  $[\text{ZnS}]_4$  layer in the crystal.

Furthermore, the element states and chemical composition of the NiIn-ZIS and ZIS are investigated by X-ray photoelectron spectroscopy (XPS) [44,45,48]. The binding energy of ZIS at 1022.35 eV and 1045.34 eV correspond to  $\text{Zn } 2p^{1/2}$  and  $\text{Zn } 2p^{3/2}$ , while the peaks position of Zn for NiIn-ZIS shift to 1022.70 eV and 1045.79 eV (Fig. 4b). The 0.35 eV positive shift confirms the In atoms successfully dope in the tetrahedral Zn sites, which is in accord with the XAFS results. The In 3d XPS spectra (Fig. 4c) demonstrate that the binding energies of In 3d<sub>5/2</sub> (445.1 eV) and In 3d<sub>3/2</sub> (452.6 eV) in NiIn-ZIS are lower than those of In 3d<sub>5/2</sub> (445.3 eV) and In 3d<sub>3/2</sub> (452.8 eV) in ZIS. Due to the higher electronegativity of In than that of Zn (the electronegativity of Zn and In is 1.65 and 1.78), In doping in tetrahedral Zn sites shows the lower electron-donating ability to the adjacent S atoms. However, compared with S 2p spectra for ZIS ( $2p^{3/2}$  161.99 eV and  $2p^{1/2}$  163.21 eV), the binding energy of S 2p spectra for NiIn-ZIS shifts to low binding energy [162.94 eV ( $\text{S } 2p^{1/2}$ ) and 161.75 eV ( $\text{S } 2p^{3/2}$ )]. Combined with the XAFS results, In and Ni doping cause the electron redistribution in NiIn-ZIS, which further affect the photocatalytic property.

### 3.2. Optimized structure and DFT calculation

The density functional theory (DFT) calculations elucidate the function of Ni and In doping on the electronic structure of the ultrathin NiIn-ZIS nanosheets. In the hexagonal  $\text{ZnIn}_2\text{S}_4$ , Zn atom connects to four S atoms to constitute a tetrahedron ( $[\text{ZnS}]_4$ ) and In atoms are octahedral- and tetrahedral- coordinated with S atoms, respectively ( $[\text{InS}]_4$  and  $[\text{InS}]_6$ ). The tetrahedron  $[\text{ZnS}]_4$  connects with octahedron  $\text{InS}_6$  by sharing S atom and the  $[\text{InS}]_6$  octahedron and  $[\text{InS}]_4$  tetrahedron are linked together by a S atom (Fig. 5a) [21,26,45,49]. The optimized geometric structure of half-unit-cell In-ZIS is shown in Fig. 5b. The electrostatic potential has a profound impact on the migration direction and enrichment behavior of electrons. As shown in Fig. 5c, series

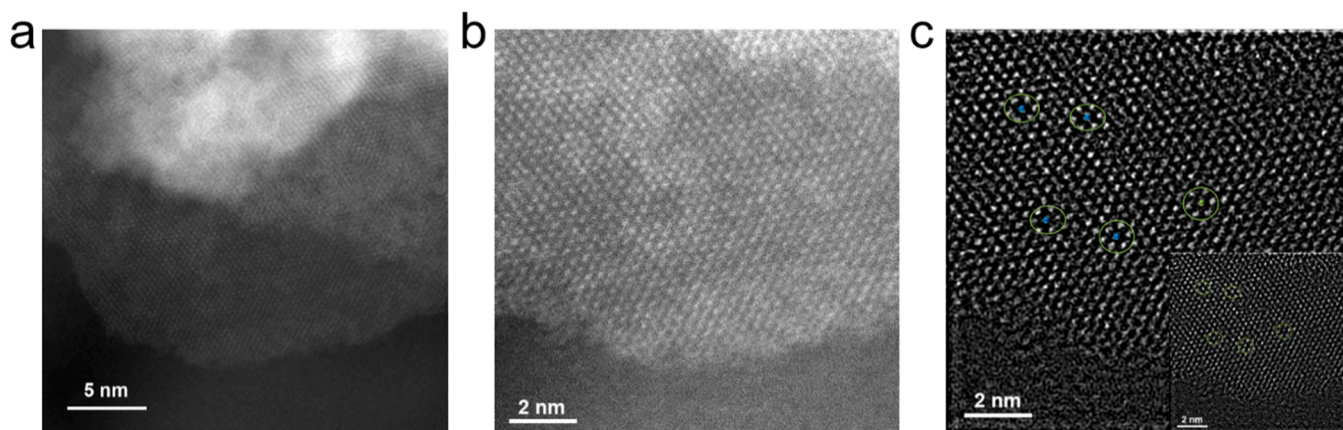
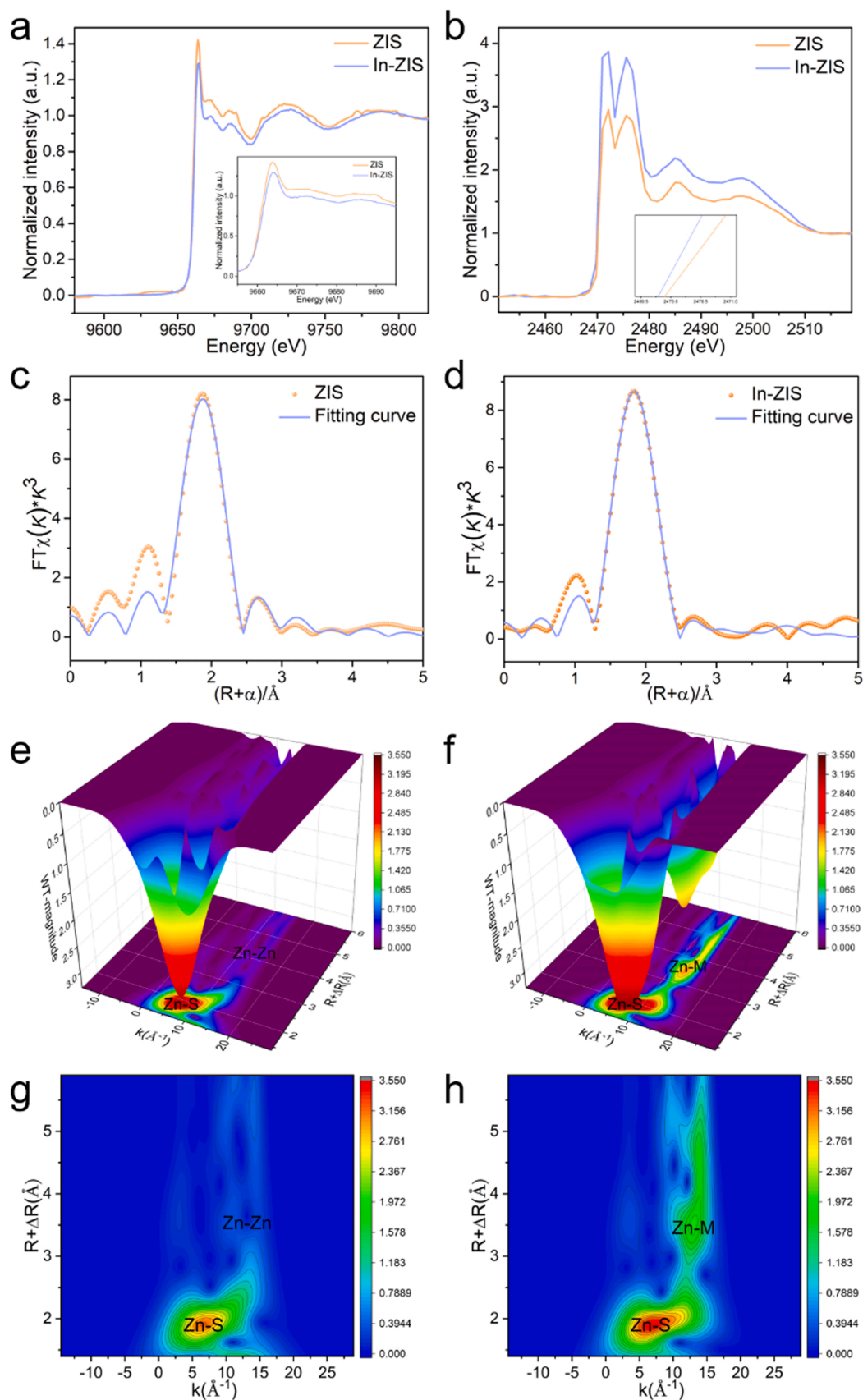


Fig. 2. Characterizations for NiIn-ZnIn<sub>2</sub>S<sub>4</sub> obtained by microwave assisted solvothermal method. (a) HAADF-STEM images and (b-c) the magnified image.





**Fig. 3.** (a) The normalized Zn K-edge XANES spectra, (b) The normalized S K-edge XANES spectra, (c), (d) the EXAFS fitting curves in R space of ZIS and In-ZIS, (e), (g) the wavelet transform (WT) contour plots of ZIS, and (f), (h) the wavelet transform (WT) contour plots of In-ZIS.

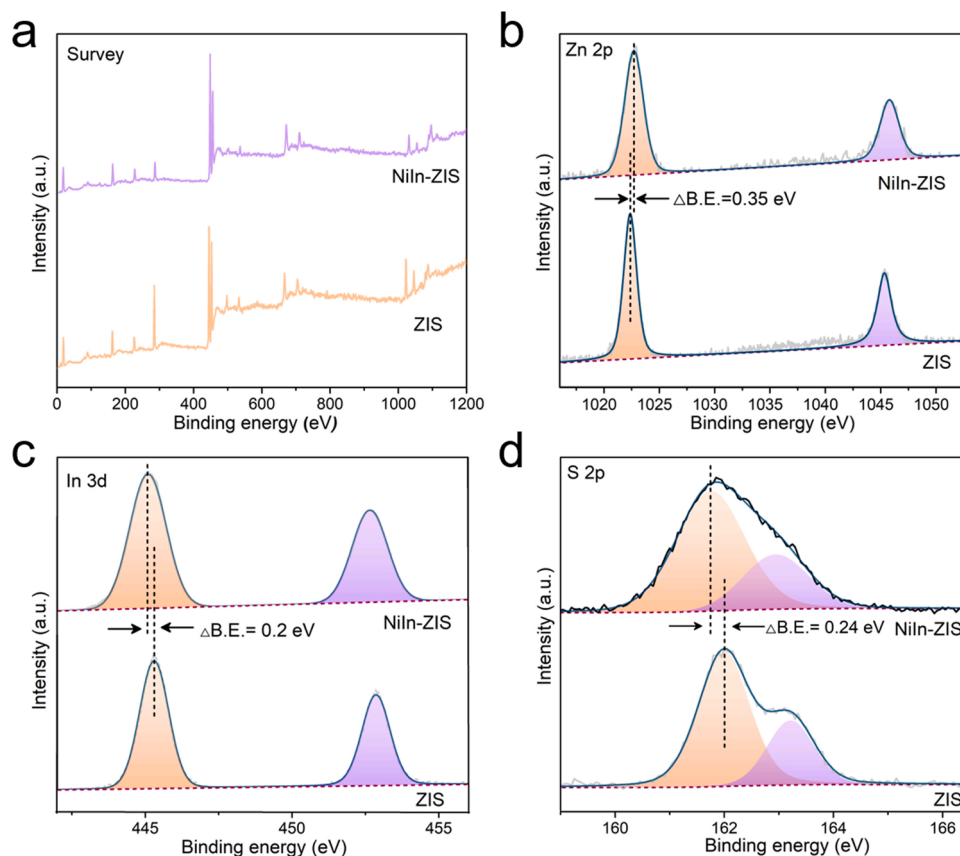


Fig. 4. XPS spectra. (a) survey, (b) Zn 2p, (c) In 3d and (d) S 2p for ZIS and In-ZIS.

potential wells block the photogenerated charges migrating from valence band ( $[\text{ZnS}]_4$  layer) to the conduction band ( $[\text{InS}]_4$  layer) along the Z axis. After In doped into ZIS, the charge density distribution of In-ZIS indicates that the delocalized of electrons around the In sites increase (Fig. S9, 10) [50–53]. Therefore, the depth of the potential wells in the Zn-S-In interlayer were decreased greatly (Fig. 5d). As a result, the In substitution with Zn in In-ZIS endow a flat transmission path for the photoexcited electron, promoting the electron rapid transfer to the active sites. After Ni doped in In-ZIS, the potential wells of NiIn-ZIS are similar as that of In-ZIS (Fig. S11b), which means In doping shows negligible effect on the potential wells. The calculated density of state (DOS) further reveals In doping elevates the Fermi levels into the conduction band and show the properties of a degenerated semiconductor [54,55] (Fig. 5e and f). As a result, the degenerated In-ZIS, attracting plenty of electrons in the conduction band, greatly enhances the electrical conductivity. Compared with the In-ZIS, the calculated DOS of NiIn-ZIS shows Ni doping induces a new impurity level on NiIn-ZIS, which can provide additional photoexcited electrons to participate the  $\text{H}_2$  evolution (Fig. S11a). Meanwhile, the calculated work function of ZIS, In-ZIS and NiIn-ZIS are 6.55 eV, 5.52 and 5.81 eV (versus vacuum level), respectively (Fig. S12), which suggests the Ni and In doping significantly reduce the work function and promote the electrons escaping from the catalyst surface to participate the reaction [56].

Besides the charge separation and transport efficiency, the H adsorption and desorption properties on S sites of ZIS is another key factor affecting performance [44,51]. From the atomic Mulliken charges and overlap populations analysis, the Mulliken charge of S sites in In-ZIS is negative than that in ZIS (Fig. 6c and Fig. S13), which inhibited the H adsorption. To improve the H adsorption on S sites, the Ni dopants were introduced to modulate the H adsorption and desorption. Owing to the lower electron-donating ability of Ni versus Zn, the S sites gain less electrons after Ni doping, which enhance H adsorption capacity on S

sites and make for the hydrogen evolution reaction. On the other side, Gibbs free energy of the intermediate state ( $\Delta G_{\text{H}}^*$ ), represent the H adsorption/desorption capabilities, is an essential indicator related to the HER performance. As shown in Fig. 6b, the calculated  $\Delta G_{\text{H}}^*$  results demonstrate the NiIn-ZIS catalyst offer a moderate  $\Delta G_{\text{H}}^*$  (0.19 eV) with respect to In-ZIS ( $\Delta G_{\text{H}}^* = 0.97$  eV) and ZIS ( $\Delta G_{\text{H}}^* = -0.36$  eV). The optimized H adsorption and desorption capabilities of NiIn-ZIS is beneficial for the photocatalytic  $\text{H}_2$  evolution. In summary, the optimized electronic potential, favorable conductivity and moderate H adsorption/desorption significantly improve the photocatalytic performances.

### 3.3. Photoelectric properties of the photocatalysts

The optical property and band structures of the ZIS samples are measured by the UV-vis diffuse reflection spectra (DRS) and Mott-Schottky plots [57–59]. As depicted in Fig. S14a, UV-vis absorption edge of NiIn-ZIS shows slight red-shift. Meanwhile, the calculated band gap ( $E_{\text{g}}$ ) of ZIS and NiIn-ZIS are 2.62 and 2.60 eV, respectively (Fig. S14b). Thus, the NiIn-ZIS shows an outstanding visible-light response. Furthermore, the flat band potential of ZIS and Ni-ZIS are  $-0.66$  V and  $-0.64$  V, respectively (Fig. S14c), suggesting the photo-generated electrons guarantee strong reduction abilities to participate the reaction. The band gap structures of all samples are listed on Fig. S14d. Except for the suitable band structure, photoexcited electrons transfer also is essential for an excellent photoreduction catalyst. Compared with ZIS, the decrease PL intensity of NiIn-ZIS reveals the In dopant efficiently prevented photogenerated charge recombination (Fig. 7a). Meanwhile, the average emission lifetime is extended from 5.31 ns of ZIS to 6.19 ns of NiIn-ZIS (Fig. 7b), which suggests the charge recombination is suppressed and the longtime photoelectrons properly participate the  $\text{H}_2$  evolution. The photocurrent density of NiIn-ZIS is

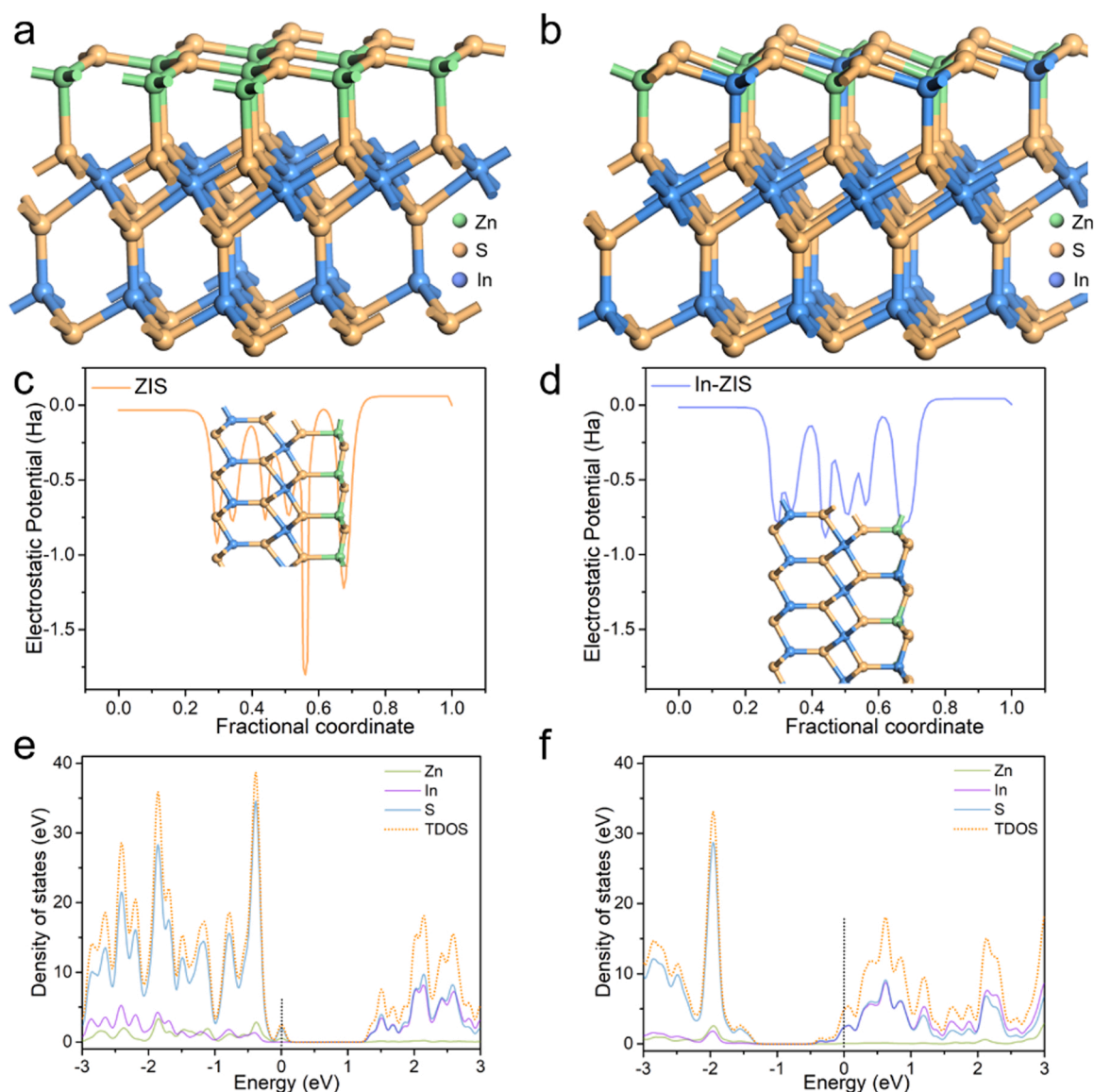


Fig. 5. (a), (b) The structural model (Zn: green, In: blue, S: yellow), (c) (d) The electrostatic potential, (e) (f) The DOS of ZIS and In-ZIS.

significantly strengthened than that of ZIS (Fig. 7c). On the other hand, the EIS result verifies NiIn-ZIS with enhanced electronic conductivity (Fig. 7d), which is consistent well with the photocurrent results. The increased photocurrent intensity and smaller electrochemical impedance indicate an improved charge separation efficiency and reduced charge-transfer resistance, which endow the excellent catalytic performance of NiIn-ZIS.

### 3.4. Photocatalytic $H_2$ evolution performance analysis

The photocatalytic  $H_2$  evolution performance of the catalyst was examined in aqueous solution containing sacrificial agent (10 vol% triethanolamine, TEOA) under visible light irradiation ( $\lambda > 420$  nm) without co-catalyst [29]. As shown in Fig. 8a, ZIS exhibits a  $H_2$  generation rate of  $3.6 \mu\text{mol}\cdot\text{h}^{-1}$ . The In substitution decreases potential wells and improves the electronic conductivity, thus the recombination of photogenerated charge is suppressed. Therefore, In-ZIS exhibits a  $H_2$  generation rate of  $11.78 \mu\text{mol}\cdot\text{h}^{-1}$ . From the thermodynamic, the H adsorption and desorption deeply affect the photocatalytic performance. Hence, the Ni dopants further substituting Zn decrease the negative charge of the S sites, balancing the H adsorption and desorption based on

In-ZIS. The optimized NiIn-ZIS showed the  $H_2$  generation rate of  $21.94 \mu\text{mol}\cdot\text{h}^{-1}$ , which was approximately 6 and 1.86 times of ZIS and In-ZIS, respectively. The apparent quantum efficiency (AQE) reaches 0.148% ( $\lambda = 400$  nm) and the trend of AQE is in agreement with the UV-vis absorption spectrum (Fig. 8c) [29,60]. As shown in Fig. 8b, the  $H_2$  generation on NiIn-ZIS presents a nearly linear relationship over time. Besides the outstanding photocatalytic activity, NiIn-ZIS catalysts also exhibits remarkable stability. The photocatalytic activity of NiIn-ZIS catalyst retains 93% after 5 cycles (Fig. 8d) and the recycled catalyst maintains the similar morphology and crystal structure (Fig. S14). XPS results of recycled catalyst also confirm that the NiIn-ZIS is stable during the cyclic reaction (Fig. S15). The In and Ni dopants in the ZIS show a synergistic effect on promoting the photogenerated carriers transfer and modulating the H absorption, thus achieving high HER performance.

## 4. Conclusion

In conclusion, Ni, In co-doped  $\text{ZnIn}_2\text{S}_4$  as highly effective photocatalyst for HER was fabricated by a microwave-assisted solvothermal synthesis method. The rapid crystallization results in the In doped in the tetrahedral Zn sites of  $\text{ZnIn}_2\text{S}_4$  during the formation of  $[\text{ZnS}]_4$  layer and



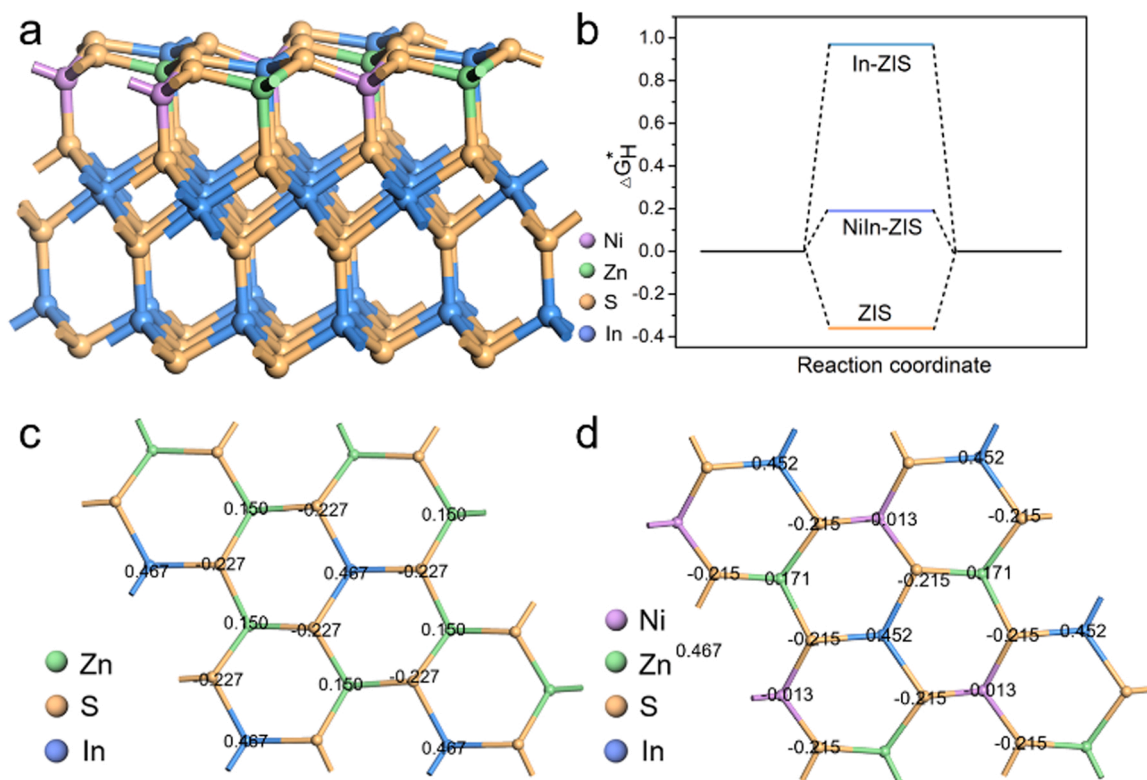


**Fig. 6.** (a) The structural model of NiIn-ZIS (Zn: green, In: blue, S: yellow, Ni: purple), (b) Hydrogen adsorption free energy of ZIS, In-ZIS and NiIn-ZIS, (c) (d) The atomic Mulliken charges of S atoms before and after Ni doping.

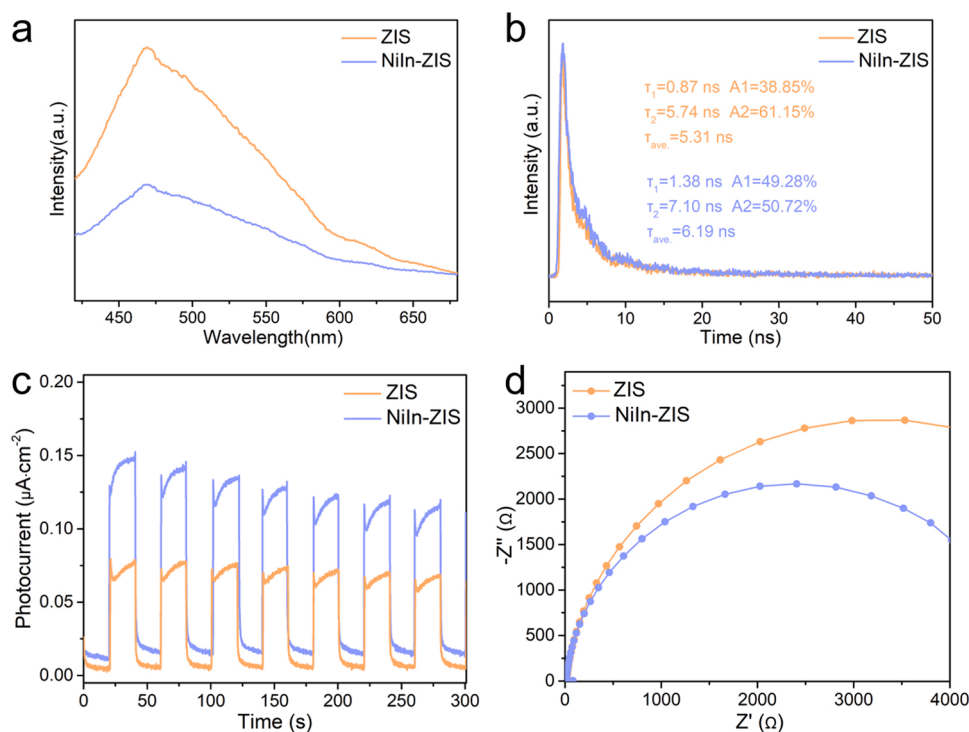


**Fig. 7.** (a) PL spectra, (b) TRPL decay spectra, (c) Photocurrent responses, (d) EIS of ZIS and NiIn-ZIS.

local disordered structures in crystal. The In doping reduces the electronic potential wells and improves electronic conductivity, which promote the separation and transport of photogenerated charges. Further, Ni doping in the tetrahedral Zn sites decreases the negative

charge on the S sites, moderates hydrogen adsorption on the S sites and improves the photocatalytic  $H_2$  evolution property. The optimized Ni, In co-doped  $ZnIn_2S_4$  achieves a superior photocatalytic activity with a HER rate of  $21.94 \mu\text{mol}\cdot\text{h}^{-1}$ , which was approximately 6 and 1.86 times of

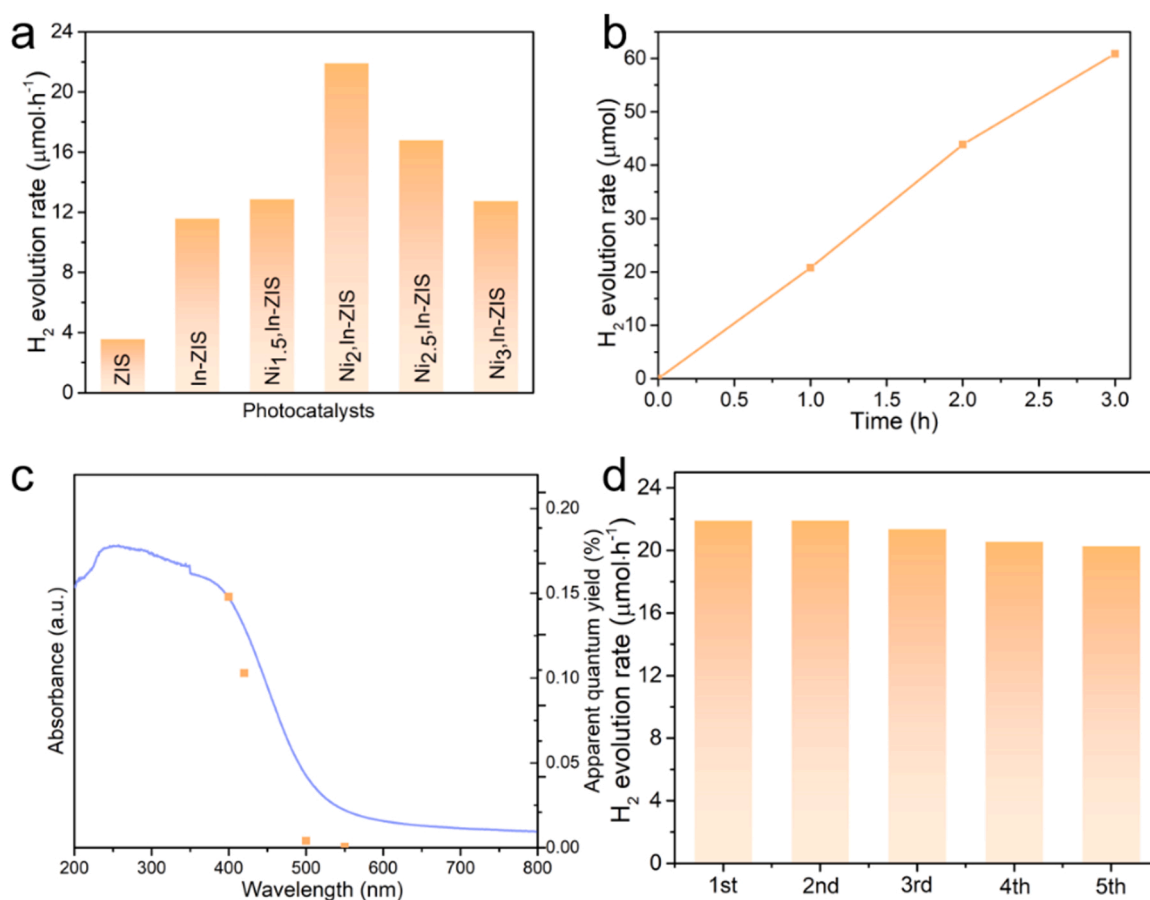


**Fig. 8.** (a) H<sub>2</sub> evolution rates of different samples, (b) Time course of H<sub>2</sub> evolution for NiIn-ZIS, (c) Apparent quantum efficiencies of NiIn-ZIS under different monochromatic light irradiation (400 nm, 420 nm, 500 nm and 550 nm), (d) Cyclic tests of NiIn-ZIS.

ZIS (3.6 μmol·h<sup>-1</sup>) and In-ZIS (11.78 μmol·h<sup>-1</sup>), respectively. This doping strategy provides a new design to promote the photocatalytic hydrogen performance.

#### CRediT authorship contribution statement

**Dongxue Zhou** conducted experiments, characterization, analysis and paper writing. **Xiangdong Xue** performed theoretical calculation and writing-editing paper. **Wenjun Dong** designed the experiments, the article structure, and revised the paper. **Xing Wang, Qingjie Luan, Liguang Zhang, Baozhen Li and Changmin Hou** performed characterization and analysis. **Ang Li and Ge Wang** revised the paper. All authors contributed to the interpretation of the results and improvement of the paper.

#### Declaration of Competing Interest

The authors declare that they have no known competing financial interests or personal relationships that could have appeared to influence the work reported in this paper.

#### Acknowledgements

This work was supported by the National Natural Science Foundation of China Natural (52071027, 51872025), the National Key R&D Program of China (2021YFB3802200), Capital's Funds for Healthcare Research and Quality Program (2021-1G-4291), Beijing Natural Science Foundation China (2212038), Natural Science Foundation of Guangdong Province (2022A1515011852), the National Defense Basic Scientific Research Defense (JCKY2021110B206), Scientific and

Technological Innovation Foundation of Foshan Scientific (BK21BE008). The computing work was supported by USTB MatCom of Beijing Advanced Innovation Center for Materials Genome Engineering.

#### Appendix A. Supporting information

Supplementary data associated with this article can be found in the online version at [doi:10.1016/j.apcatb.2022.121337](https://doi.org/10.1016/j.apcatb.2022.121337).

#### References

- [1] T. Hisatomi, K.J.N.C. Domen, Reaction systems for solar hydrogen production via water splitting with particulate semiconductor photocatalysts, *Nat. Catal.* 2 (2019) 387–399, <https://doi.org/10.1038/s41929-019-0242-6>.
- [2] N. Luo, T. Montini, J. Zhang, P. Fornasiero, E. Fonda, T. Hou, W. Nie, J. Lu, J. Liu, M. Heggen, L. Lin, C. Ma, M. Wang, F. Fan, S. Jin, F. Wang, Visible-light-driven coproduction of diesel precursors and hydrogen from lignocellulose-derived methylfurans, *Nat. Energy* 4 (2019) 575–584, <https://doi.org/10.1038/s41560-019-0403-5>.
- [3] Q. Wang, K. Domen, Particulate photocatalysts for light-driven water splitting: mechanisms, challenges and design strategies, *Chem. Rev.* 120 (2020) 919–985, <https://doi.org/10.1021/acs.chemrev.9b00201>.
- [4] Y. Wang, H. Suzuki, J. Xie, O. Tomita, D.J. Martin, M. Higashi, D. Kong, R. Abe, J. Tang, Mimicking natural photosynthesis: solar to renewable H<sub>2</sub> fuel synthesis by Z-Scheme water splitting systems, *Chem. Rev.* 118 (2018) 5201–5241, <https://doi.org/10.1021/acs.chemrev.7b00286>.
- [5] Y. He, D. Wang, Toward practical solar hydrogen production, *Chem* 4 (2018) 405–408, <https://doi.org/10.1016/j.chempr.2018.02.013>.
- [6] C. Gu, H.M. Xu, S.K. Han, M.R. Gao, S.H. Yu, Soft chemistry of metastable metal chalcogenide nanomaterials, *Chem. Soc. Rev.* 50 (2021) 6671–6683, <https://www.ncbi.nlm.nih.gov/pubmed/33942832>.
- [7] Y. Liu, H. Wang, X. Yuan, Y. Wu, H. Wang, Y.Z. Tan, J.W. Chew, Roles of sulfur-edge sites, metal-edge sites, terrace sites, and defects in metal sulfides for photocatalysis, *Chem. Catal.* 1 (2021) 44–68, <https://doi.org/10.1016/j.checat.2021.01.002>.

- [8] J. Wang, S. Lin, N. Tian, T. Ma, Y. Zhang, H. Huang, Nanostructured metal sulfides: classification, modification strategy, and solar-driven CO<sub>2</sub> reduction application, *Adv. Funct. Mater.* 31 (2020), <https://doi.org/10.1002/adfm.202008008>.
- [9] B. Xiao, T. Lv, J. Zhao, Q. Rong, H. Zhang, H. Wei, J. He, J. Zhang, Y. Zhang, Y. Peng, Q. Liu, Synergistic effect of the surface vacancy defects for promoting photocatalytic stability and activity of ZnS nanoparticles, *ACS Catal.* 11 (2021) 13255–13265, <https://doi.org/10.1021/acscatal.1c03476>.
- [10] E. Zhang, Q. Zhu, J. Huang, J. Liu, G. Tan, C. Sun, T. Li, S. Liu, Y. Li, H. Wang, X. Wan, Z. Wen, F. Fan, J. Zhang, K. Ariga, Visually resolving the direct Z-scheme heterojunction in CdS@ZnIn<sub>2</sub>S<sub>4</sub> hollow cubes for photocatalytic evolution of H<sub>2</sub> and H<sub>2</sub>O<sub>2</sub> from pure water, *Appl. Catal. B-Environ.* 293 (2021), <https://doi.org/10.1016/j.apcatb.2021.120213>.
- [11] Y. Chen, G. Tian, W. Zhou, Y. Xiao, J. Wang, X. Zhang, H. Fu, Enhanced photogenerated carrier separation in CdS quantum dot sensitized ZnFe<sub>2</sub>O<sub>4</sub>/ZnIn<sub>2</sub>S<sub>4</sub> nanosheet stereoscopic films for exceptional visible light photocatalytic H<sub>2</sub> evolution performance, *Nanoscale* 9 (2017) 5912–5921, <https://www.ncbi.nlm.nih.gov/pubmed/28436507>.
- [12] Q. Sun, N. Wang, J. Yu, J.C. Yu, A hollow porous CdS photocatalyst, *Adv. Mater.* (2018), e1804368, <https://doi.org/10.1002/adma.201804368>.
- [13] X.-L. Yin, L.-L. Li, M.-L. Liu, D.-C. Li, L. Shang, J.-M. Dou, MoS<sub>2</sub>/CdS nano-heterostructures accurately constructed on the defects of CdS for efficient photocatalytic H<sub>2</sub> evolution under visible light irradiation, *Chem. Eng. J.* 370 (2019) 305–313, <https://doi.org/10.1016/j.cej.2019.03.231>.
- [14] M. Wang, G. Zhang, Z. Guan, J. Yang, Q. Li, Spatially separating redox centers and photothermal effect synergistically boosting the photocatalytic hydrogen evolution of ZnIn<sub>2</sub>S<sub>4</sub> nanosheets, *Small* 17 (2021), e2006952, <https://doi.org/10.1002/smll.202006952>.
- [15] S. Wang, B.Y. Guan, X. Wang, X.W.D. Lou, Formation of hierarchical Co<sub>9</sub>S<sub>8</sub>@ZnIn<sub>2</sub>S<sub>4</sub> heterostructured cages as an efficient photocatalyst for hydrogen evolution, *J. Am. Chem. Soc.* 140 (2018) 15145–15148, <https://doi.org/10.1021/jacs.8b07721>.
- [16] Y. Chao, P. Zhou, J. Lai, W. Zhang, H. Yang, S. Lu, H. Chen, K. Yin, M. Li, L. Tao, C. Shang, M. Tong, S. Guo, Ni<sub>1-x</sub>Co<sub>x</sub>Se<sub>2</sub>-C/ZnIn<sub>2</sub>S<sub>4</sub> hybrid nanocages with strong 2D/2D hetero-interface interaction enable efficient H<sub>2</sub>-releasing photocatalysis, *Adv. Funct. Mater.* 31 (2021) 2100923, <https://doi.org/10.1002/adfm.202100923>.
- [17] Y. Kumar, R. Kumar, P. Raizada, A.A.P. Khan, Q.V. Le, P. Singh, V.-H. Nguyen, Novel Z-Scheme ZnIn<sub>2</sub>S<sub>4</sub>-based photocatalysts for solar-driven environmental and energy applications: progress and perspectives, *J. Mater. Sci. Technol.* 87 (2021) 234–257, <https://doi.org/10.1016/j.jmst.2021.01.051>.
- [18] J. Wang, S. Sun, R. Zhou, Y. Li, Z. He, H. Ding, D. Chen, W. Ao, A review: synthesis, modification and photocatalytic applications of ZnIn<sub>2</sub>S<sub>4</sub>, *J. Mater. Sci. Technol.* 78 (2021) 1–19, <https://doi.org/10.1016/j.jmst.2020.09.045>.
- [19] G. Zhang, D. Chen, N. Li, Q. Xu, H. Li, J. He, J.J.A.C. Lu, Construction of hierarchical hollow Co<sub>9</sub>S<sub>8</sub>/ZnIn<sub>2</sub>S<sub>4</sub> tubular heterostructures for highly efficient solar energy conversion and environmental remediation, *Angew. Chem. Int. Ed. Engl.* 132 (2020) 8332–8338, <https://doi.org/10.1002/ange.202000503>.
- [20] P. Wang, Z. Shen, Y. Xia, H. Wang, L. Zheng, W. Xi, S. Zhan, Atomic insights for optimum and excess doping in photocatalysis: a case study of few-layer Cu-ZnIn<sub>2</sub>S<sub>4</sub>, *Adv. Funct. Mater.* 29 (2019) 1807013, <https://doi.org/10.1002/adfm.201807013>.
- [21] X. Jiao, Z. Chen, X. Li, Y. Sun, S. Gao, W. Yan, C. Wang, Q. Zhang, Y. Lin, Y. Luo, Y. Xie, Defect-mediated electron-hole separation in one-unit-cell ZnIn<sub>2</sub>S<sub>4</sub> layers for boosted solar-driven CO<sub>2</sub> reduction, *J. Am. Chem. Soc.* 139 (2017) 7586–7594, <https://doi.org/10.1021/jacs.7b02290>.
- [22] K. Ding, Y. Li, B. Chen, Y. Zhang, Original investigation of a novel photocatalyst driven by visible light: ZnIn<sub>2</sub>S<sub>4</sub>, *J. Phys. Soc.* 83 (2014), 074301, <https://doi.org/10.7566/JPSJ.83.074301>.
- [23] G. Wang, G. Chen, Y. Yu, X. Zhou, Y. Teng, Mixed solvothermal synthesis of hierarchical ZnIn<sub>2</sub>S<sub>4</sub> spheres: specific facet-induced photocatalytic activity enhancement and a DFT elucidation, *RSC Adv.* 3 (2013) 18579–18586, <https://doi.org/10.1039/c3ra42245c>.
- [24] W. Yang, X.-L. Wang, N. Kong, C. Liu, P. Sun, Z. Wang, Y. Ding, H. Lin, D. Li, T. Wu, Minimized external electric field on asymmetric monolayer maximizes charge separation for photocatalysis, *Appl. Catal. B-Environ.* 295 (2021), <https://doi.org/10.1016/j.apcatb.2021.120266>.
- [25] S. Zhang, X. Liu, C. Liu, S. Luo, L. Wang, T. Cai, Y. Zeng, J. Yuan, W. Dong, Y. Pei, Y. Liu, MoS<sub>2</sub> quantum dot growth induced by S vacancies in a ZnIn<sub>2</sub>S<sub>4</sub> monolayer: atomic-level heterostructure for photocatalytic hydrogen production, *ACS Nano* 12 (2018) 751–758, <https://doi.org/10.1021/acsnano.7b07974>.
- [26] S. Zhang, Z. Zhang, Y. Si, B. Li, F. Deng, L. Yang, X. Liu, W. Dai, S. Luo, Gradient hydrogen migration modulated with self-adapting S vacancy in copper-doped ZnIn<sub>2</sub>S<sub>4</sub> nanosheet for photocatalytic hydrogen evolution, *ACS Nano* 15 (2021) 15238–15248, <https://doi.org/10.1021/acsnano.1c05834>.
- [27] G. Zuo, Y. Wang, W.L. Teo, A. Xie, Y. Guo, Y. Dai, W. Zhou, D. Jana, Q. Xian, W. Dong, Y. Zhao, Ultrathin ZnIn<sub>2</sub>S<sub>4</sub> nanosheets anchored on Ti<sub>3</sub>C<sub>2</sub>T<sub>x</sub> MXene for photocatalytic H<sub>2</sub> evolution, *Angew. Chem. Int. Ed. Engl.* 59 (2020) 11287–11292, <https://doi.org/10.1002/anie.202002136>.
- [28] F. Xing, C. Cheng, J. Zhang, Q. Liu, C. Chen, C. Huang, Tunable charge transfer efficiency in H<sub>2</sub>MoO<sub>3</sub>@ZnIn<sub>2</sub>S<sub>4</sub> hierarchical direct Z-scheme heterojunction toward efficient visible-light-driven hydrogen evolution, *Appl. Catal. B-Environ.* 285 (2021), 119818, <https://doi.org/10.1016/j.apcatb.2020.119818>.
- [29] C. Du, Q. Zhang, Z. Lin, B. Yan, C. Xia, G. Yang, Half-unit-cell ZnIn<sub>2</sub>S<sub>4</sub> monolayer with sulfur vacancies for photocatalytic hydrogen evolution, *Appl. Catal. B-Environ.* 248 (2019) 193–201, <https://doi.org/10.1016/j.apcatb.2019.02.027>.
- [30] Q. Han, X. Bai, Z. Man, H. He, L. Li, J. Hu, A. Alsaedi, T. Hayat, Z. Yu, W. Zhang, J. Wang, Y. Zhou, Z. Zou, Convincing synthesis of atomically thin, single-crystalline InVO<sub>4</sub> sheets toward promoting highly selective and efficient solar conversion of CO<sub>2</sub> into CO, *J. Am. Chem. Soc.* 141 (2019) 4209–4213, <https://doi.org/10.1021/jacs.8b13673>.
- [31] Q. Zhang, H. Gu, X. Wang, L. Li, J. Zhang, H. Zhang, Y.-F. Li, W.-L. Dai, Robust hollow tubular ZnIn<sub>2</sub>S<sub>4</sub> modified with embedded metal-organic-framework-layers: extraordinarily high photocatalytic hydrogen evolution activity under simulated and real sunlight irradiation, *Appl. Catal. B-Environ.* 298 (2021), 120632, <https://doi.org/10.1016/j.apcatb.2021.120632>.
- [32] X. Cai, Z. Zeng, Y. Liu, Z. Li, X. Gu, Y. Zhao, L. Mao, J. Zhang, Visible-light-driven water splitting by yolk-shelled ZnIn<sub>2</sub>S<sub>4</sub>-based heterostructure without noble-metal co-catalyst and sacrificial agent, *Appl. Catal. B-Environ.* 297 (2021), 120391, <https://doi.org/10.1016/j.apcatb.2021.120391>.
- [33] A. Faucher, V.V. Tersikh, R.E. Wasylishen, Feasibility of arsenic and antimony NMR spectroscopy in solids: an investigation of some group 15 compounds, *Solid State Nucl. Magn. Reson.* 61 (2014) 54–61, <https://doi.org/10.1016/j.ssnmr.2014.05.005>.
- [34] M.D.S. Stewart, J. Clark, Chris J. Pickard, Phil J. Hasnip, Matt I.J. Probert, Keith Refson, Mike C. Payne, First principles methods using CASTEP, *Z. Kristallogr.* 220 (2005) 567–570, <https://doi.org/10.1524/zkri.220.5.567.65075>.
- [35] M.C. Payne, M.P. Teter, D.C. Allan, T.A. Arias, J.D. Joannopoulos, Iterative minimization techniques for ab initio total-energy calculations: molecular dynamics and conjugate gradients, *Rev. Mod. Phys.* 64 (1992) 1045–1097, <https://doi.org/10.1103/RevModPhys.64.1045>.
- [36] S. Shen, L. Zhao, Z. Zhou, L. Guo, Enhanced photocatalytic hydrogen evolution over Cu-doped ZnIn<sub>2</sub>S<sub>4</sub> under visible light irradiation, *J. Phys. Chem. C* 112 (2008) 16148–16155, <https://doi.org/10.1021/jp804525q>.
- [37] M.B. Schütz, L. Xiao, T. Lehnen, T. Fischer, S. Mathur, Microwave-assisted synthesis of nanocrystalline binary and ternary metal oxides, *Int. Mater. Rev.* 63 (2017) 341–374, <https://doi.org/10.1080/09506608.2017.1402158>.
- [38] I. Bilecka, M. Niederberger, Microwave chemistry for inorganic nanomaterials synthesis, *Nanoscale* 2 (2010) 1358–1374, <https://doi.org/10.1016/10.1039/b9nr00377k>.
- [39] S. Shen, J. Chen, X. Wang, L. Zhao, L. Guo, Microwave-assisted hydrothermal synthesis of transition-metal doped ZnIn<sub>2</sub>S<sub>4</sub> and its photocatalytic activity for hydrogen evolution under visible light, *J. Power Sources* 196 (2011) 10112–10119, <https://doi.org/10.1016/j.jpowsour.2011.08.103>.
- [40] T.V. de Medeiros, J. Manioudakis, F. Noun, J.-R. Macairan, F. Victoria, R. Naccache, Microwave-assisted synthesis of carbon dots and their applications, *J. Mater. Chem. C* 7 (2019) 7175–7195, <https://doi.org/10.1039/c9tc01640f>.
- [41] Q. Luan, X. Xue, R. Li, L. Gu, W. Dong, D. Zhou, X. Wang, B. Li, G. Wang, C. Hou, Boosting photocatalytic hydrogen evolution: orbital redistribution of ultrathin ZnIn<sub>2</sub>S<sub>4</sub> nanosheets via atomic defects, *Appl. Catal. B-Environ.* 305 (2022), 121007, <https://doi.org/10.1016/j.apcatb.2021.121007>.
- [42] Z. Wang, M. Saito, K.P. McKenna, L. Gu, S. Tsukimoto, A.L. Shluger, Y. Ikuhara, Atom-resolved imaging of ordered defect superstructures at individual grain boundaries, *Nature* 479 (2011) 380–383, <https://doi.org/10.1038/nature10593>.
- [43] R. Pan, M. Hu, J. Liu, D. Li, X. Wan, H. Wang, Y. Li, X. Zhang, X. Wang, J. Jiang, J. Zhang, Two-dimensional all-in-One sulfide monolayers driving photocatalytic overall water splitting, *Nano Lett.* 21 (2021) 6228–6236, <https://doi.org/10.1021/acs.nanolett.1c02008>.
- [44] B. Qiu, P. Huang, C. Lian, Y. Ma, M. Xing, H. Liu, J. Zhang, Realization of all-in-one hydrogen-evolving photocatalysts via selective atomic substitution, *Appl. Catal. B-Environ.* 298 (2021), 120518, <https://doi.org/10.1016/j.apcatb.2021.120518>.
- [45] X. Shi, L. Mao, C. Dai, P. Yang, J. Zhang, F. Dong, L. Zheng, M. Fujitsuka, H. Zheng, Inert basal plane activation of two-dimensional ZnIn<sub>2</sub>S<sub>4</sub> via Ni atom doping for enhanced co-catalyst free photocatalytic hydrogen evolution, *J. Mater. Chem. A* 8 (2020) 13376–13384.
- [46] Y. Zhang, S. Niu, Y. Wu, X. Zheng, J. Cai, J. Ye, Y. Xie, Y. Liu, J. Zhou, J. Zhu, X. Liu, G. Wang, Y. Qian, Tuning orbital orientation endows molybdenum disulfide with exceptional alkaline hydrogen evolution capability, *Nat. Commun.* 10 (2019) 1217, <https://doi.org/10.1038/s41467-019-09210-0>.
- [47] H. Zhang, L. Yu, T. Chen, W. Zhou, X.W.D. Lou, Surface modulation of hierarchical MoS<sub>2</sub> nanosheets by Ni single atoms for enhanced electrocatalytic hydrogen evolution, *Adv. Funct. Mater.* 28 (2018), <https://doi.org/10.1002/adfm.201807086>.
- [48] A. Yan, X. Shi, F. Huang, M. Fujitsuka, T. Majima, Efficient photocatalytic H<sub>2</sub> evolution using NiS/ZnIn<sub>2</sub>S<sub>4</sub> heterostructures with enhanced charge separation and interfacial charge transfer, *Appl. Catal. B-Environ.* 250 (2019) 163–170, <https://doi.org/10.1016/j.apcatb.2019.02.075>.
- [49] M. Dong, P. Zhou, C. Jiang, B. Cheng, J. Yu, First-principles investigation of Cu-doped ZnS with enhanced photocatalytic hydrogen production activity, *Chem. Phys. Lett.* 668 (2017) 1–6, <https://doi.org/10.1016/j.cplett.2016.12.008>.
- [50] J. Li, G. Zhan, Y. Yu, L. Zhang, Superior visible light hydrogen evolution of Janus bilayer junctions via atomic-level charge flow steering, *Nat. Commun.* 7 (2016) 11480, <https://doi.org/10.1038/ncomms11480>.
- [51] Y. Cao, L. Guo, M. Dan, D.E. Doronkin, C. Han, Z. Rao, Y. Liu, J. Meng, Z. Huang, K. Zheng, P. Chen, F. Dong, Y. Zhou, Modulating electron density of vacancy site by single Au atom for effective CO<sub>2</sub> photoreduction, *Nat. Commun.* 12 (2021) 1675, <https://doi.org/10.1038/s41467-021-21925-7>.
- [52] Z.-K. Shen, M. Cheng, Y.-J. Yuan, L. Pei, J. Zhong, J. Guan, X. Li, Z.-J. Li, L. Bao, X. Zhang, Z.-T. Yu, Z. Zou, Identifying the role of interface chemical bonds in activating charge transfer for enhanced photocatalytic nitrogen fixation of Ni<sub>2</sub>P-black phosphorus photocatalysts, *Appl. Catal. B-Environ.* 295 (2021), 120274, <https://doi.org/10.1016/j.apcatb.2021.120274>.



- [53] Y. Peng, M. Geng, J. Yu, Y. Zhang, F. Tian, Yn Guo, D. Zhang, X. Yang, Z. Li, Z. Li, S. Zhang, Vacancy-induced 2H@1T MoS<sub>2</sub> phase-incorporation on ZnIn<sub>2</sub>S<sub>4</sub> for boosting photocatalytic hydrogen evolution, *Appl. Catal. B-Environ.* 298 (2021), 120570, <https://doi.org/10.1016/j.apcatb.2021.120570>.
- [54] Z. Chen, S. Wu, J. Ma, S. Mine, T. Toyao, M. Matsuoka, L. Wang, J. Zhang, Non-oxidative coupling of methane: N-type doping of niobium single atoms in TiO<sub>2</sub>-SiO<sub>2</sub> induces electron localization, *Angew. Chem. Int. Ed. Engl.* 60 (2021) 11901–11909, <https://doi.org/10.1002/anie.202016420>.
- [55] Z.H. Ge, Y. Qiu, Y.X. Chen, X. Chong, J. Feng, Z.K. Liu, J. He, Multipoint defect synergy realizing the excellent thermoelectric performance of n-Type polycrystalline SnSe via Re doping, *Adv. Funct. Mater.* 29 (2019) 1902893, <https://doi.org/10.1002/adfm.201902893>.
- [56] Z. Yang, X. Xia, W. Yang, L. wang, Y. Liu, Photothermal effect and continuous hot electrons injection synergistically induced enhanced molecular oxygen activation for efficient selective oxidation of benzyl alcohol over plasmonic W<sub>18</sub>O<sub>49</sub>/ZnIn<sub>2</sub>S<sub>4</sub> photocatalyst, *Appl. Catal. B-Environ.* 299 (2021), 120675, <https://doi.org/10.1016/j.apcatb.2021.120675>.
- [57] Z. Li, W. Huang, J. Liu, K. Lv, Q. Li, Embedding CdS@Au into ultrathin Ti<sub>3-x</sub>C<sub>2</sub>Ty to build dual schottky barriers for photocatalytic H<sub>2</sub> production, *ACS Catal.* 11 (2021) 8510–8520, <https://doi.org/10.1021/acscatal.1c02018>.
- [58] Q. Li, Y. Xia, C. Yang, K. Lv, M. Lei, M. Li, Building a direct Z-scheme heterojunction photocatalyst by ZnIn<sub>2</sub>S<sub>4</sub> nanosheets and TiO<sub>2</sub> hollowspheres for highly-efficient artificial photosynthesis, *Chem. Eng. J.* 349 (2018) 287–296, <https://doi.org/10.1016/j.cej.2018.05.094>.
- [59] Y. Xia, Q. Li, K. Lv, D. Tang, M. Li, Superiority of graphene over carbon analogs for enhanced photocatalytic H<sub>2</sub>-production activity of ZnIn<sub>2</sub>S<sub>4</sub>, *Appl. Catal. B-Environ.* 206 (2017) 344–352, <https://doi.org/10.1016/j.apcatb.2017.01.060>.
- [60] X. Peng, L. Ye, Y. Ding, L. Yi, C. Zhang, Z. Wen, Nanohybrid photocatalysts with ZnIn<sub>2</sub>S<sub>4</sub> nanosheets encapsulated UiO-66 octahedral nanoparticles for visible-light-driven hydrogen generation, *Appl. Catal. B-Environ.* 260 (2020), <https://doi.org/10.1016/j.apcatb.2019.118152>.